

## Chapter 7

### Imaging Fluorescence

We have discussed schemes designed to detect and image heterogeneities in biological tissues with diffusing near-infrared (NIR) light. These studies have centered on the detection of variations in the absorption and scattering coefficients in tissue and tissue phantoms. Recently however, fluorescent contrast agents have also been considered as a means to enhance the specificity and sensitivity in tumor detection [7, 11, 67, 68, 69, 70, 71, 33]. Fluorescent lifetime-based quantitation of different biological parameters such as tissue oxygenation  $pO_2$  [72], pH value [73] and intracellular calcium concentration  $[Ca^{2+}]$  [74] have been proposed by several investigators. Localized fluorophore concentration

may signal an increased number of small blood vessels associated with rapid tumor growth [75]. The altered concentration of a fluorophore quencher (such as oxygen) which affects the fluorophore lifetime may signal the high oxygen uptake in a rapidly growing tumor [76]. Thus functional imaging of the variations of fluorophore concentration and lifetime may provide useful clinical information.

Much effort has been devoted to formulate the forward problem of fluorescent light in turbid media. An integral form in the time domain has been given by Hutchinson *et al.* for the migration of fluorescent light in turbid media; these investigators have also numerically solved this integral equation in specific two-dimensional homogeneous and heterogeneous systems [21, 77]. A mathematical model for frequency domain fluorescent light propagation in semi-infinite homogeneous turbid media has been obtained by Patterson *et al.* using zero boundary conditions and assuming that

the reduced scattering coefficients are the same for the excitation and emission light [68]. A useful algorithm has been developed by Wu *et al.* to deconvolve fluorescent emission spectra from tissue reflectance measurements [78]. Finally, in our lab, Li *et al.* [79] have presented analytic solutions for fluorescent diffuse photon density waves in homogeneous and heterogeneous turbid media with planar boundaries. The frequency domain analysis can easily be applied to time domain experiments by Fourier transformation of the time domain data.

In this chapter we will first discuss the equations which describe the passage of photons through a fluorescent medium. Next we examine the limited case in which we wish to detect and localize the center of a fluorescent object. Finally, we turn our attention to the more complicated problem of tomographic image reconstruction techniques for fluorescence lifetime imaging in turbid media [12].

Identifying and localizing a tumor becomes a simple procedure if we can turn a tumor into a source using exogenous fluorescent contrast agents. Although there are currently no FDA approved fluorescent contrast agents which specifically bind to tumor sites, the rapid growth of a tumor results in increased vascularity in the region and an abundance of leaky blood vessels. Certain molecules, such as the popular MRI contrast agent gadolinium chelate, are known to leak from blood vessels and accumulate in the intravascular space. Other contrast agents of the same molecular size, such as indo cyanine green (ICG) are expected to similarly accumulate at the tumor site. Preliminary studies show a three fold increase in the amount of ICG in rat tumor compared to normal tissue [70]. ICG is an excellent choice for NIR imaging since it has an absorption peak at 780 nm, fluoresces at 830 nm, and is currently used in humans to test hepatic and cardiac function [80].

## 7.1 Fluorescent Diffuse Photon Density Wave Theory

In this section we will develop the theory of diffusive waves propagating through fluorescent media. In this analysis, the fluorescent radiation is assumed to be well separated in energy from that of incident photons so that we safely ignore the possi-

bility of the excitation of fluorophores by the fluorescent re-emission. We also assume that the excited fluorophores have a single lifetime. We will treat fluorophore and chromophore absorptions separately, and we assume the change of scattering coefficient due to the fluorophore is negligible for the notational simplicity (however the fluorophore scattering effect is easily incorporated). Absorption due to fluorophores concentration is characterized by an additional absorption coefficient over the background,  $\sigma N_t$ , where  $N_t$  is the concentration of fluorophore and  $\sigma$  is the fluorophore absorption cross-section. Thus in the presence of fluorophores, the total absorption coefficient is the sum of the chromophore absorption coefficient plus the fluorophore absorption coefficient.

Suppose an intensity-modulated point source is at position  $\mathbf{r}_s$  in a homogeneous system. A fluorophore in the medium will be excited by the incident DPDW. The excited fluorophore then acts as a secondary point source of fluorescent diffusive waves (Fig.(1a)). Treating fluorophores as a two level quantum system and ignoring saturation effects, we find that the number of excited fluorophores,  $N$  obeys the following linear diffusion equation [70],

$$\frac{\partial N(\mathbf{r}, t)}{\partial t} = -\Gamma N(\mathbf{r}, t) + \sigma v U(\mathbf{r}, \mathbf{r}_s) e^{-i\omega t} N_t(\mathbf{r}) \quad (7.1)$$

where  $\Gamma$  is the excited dye decay rate,  $N_t$  is the number of dye molecules per unit volume at a position  $\mathbf{r}$ ,  $\sigma$  is the absorption cross section of the dye, and  $vU(\mathbf{r}, \mathbf{r}_s)e^{i\omega t}$  is the incident photon fluence at a position  $\mathbf{r}$  from a source at  $\mathbf{r}_s$ . For the case of an amplitude modulated source,  $N(\mathbf{r}, t) = N(\mathbf{r})e^{-i\omega t}$  so 7.1 can be used to obtain

$$-i\omega N(\mathbf{r}) = -\Gamma N(\mathbf{r}) + \sigma v U(\mathbf{r}, \mathbf{r}_s) N_t(\mathbf{r}) \quad (7.2)$$

$$N(\mathbf{r}) = \frac{\sigma v U(\mathbf{r}, \mathbf{r}_s) N_t(\mathbf{r})}{\Gamma - i\omega} \quad (7.3)$$

and the rate of production of fluorescent photons is

$$\Gamma N(\mathbf{r}) = \frac{\sigma v U(\mathbf{r}, \mathbf{r}_s) N_t(\mathbf{r})}{1 - i\omega\tau} \quad (7.4)$$

where  $\tau = 1/\Gamma$  is the fluorescent lifetime.

The term  $\Gamma N(\mathbf{r})$  is now a source of fluorescent diffuse photon density waves. These photons will propagate to the detector position  $\mathbf{r}_d$ , so the detected fluorescent signal is

$$u_{fl} = \Gamma N(\mathbf{r})U'(\mathbf{r}_d, \mathbf{r}) = \Gamma N(\mathbf{r})\frac{\exp(ik'|\mathbf{r}_d - \mathbf{r}|)}{4\pi|\mathbf{r}_d - \mathbf{r}|} \quad (7.5)$$

where we have written  $U'$  ( $k'$ ) instead of  $U$  ( $k$ ) as a reminder that the properties of the fluorescent DPDW are governed by the optical properties of the medium at the fluorescent wavelength. To calculate the total fluorescent signal from a homogeneous distribution of fluorophore, we integrate over all fluorophores,

$$U_{fl} = \int d\mathbf{r} \Gamma N(\mathbf{r})U'(\mathbf{r}_d, \mathbf{r}) \quad (7.6)$$

$$= \int d\mathbf{r} U(\mathbf{r}, \mathbf{r}_s)\frac{N_t(\mathbf{r})\sigma v}{1 - i\omega\tau}U'(\mathbf{r}_d, \mathbf{r}) \quad (7.7)$$

For notational simplicity, we assume excited fluorophores decay only through the radiation channel, i.e. the fluorescent yield is 100%. A fluorescent yield of less than 100% will result in an overall attenuation factor. The factor  $N_t(\mathbf{r})\sigma v$  will be written as  $\eta$ .

This process is diagramed in figure 7.1. Excitation photons pass from the source to a position within the sample. The DPDW is demodulated by a factor of  $\eta/(1 - i\omega\tau)$  due to the absorption factor and lifetime of the fluorophore, and finally the fluorophore acts as a source of fluorescent DPDW's which propagate to the detector at position  $\mathbf{r}$ . The detected fluorescent DPDW is found by integrating over all fluorescent sources.

The same solution can be derived using a time domain approach and then taking the Fourier transform of the solution (see appendix C).

In this formulation we have assumed that the emission spectra is at a single optical wavelength. In fact, a fluorophore will usually emit light over a distribution of wavelengths. In our work we have chosen to approximate the excitation and fluorescent signal as monochromatic. To properly incorporate the broad absorption and reradiation of the fluorescent dyes, we need to integrate over the wavelengths;

$$U_{fl}(\mathbf{r}_s, \mathbf{r}_d, \tau, \omega) = \int_{\lambda_1^{min}}^{\lambda_1^{max}} d\lambda_1 \int_{\lambda_2^{min}}^{\lambda_2^{max}} d\lambda_2 \int_{-\infty}^{\infty} d\mathbf{r} U_{\lambda_1}(\mathbf{r}_s, \mathbf{r}, \omega) \frac{\eta_{\lambda_1}}{1 - i\omega\tau} U'_{\lambda_2}(\mathbf{r}_d, \mathbf{r}, \omega).$$

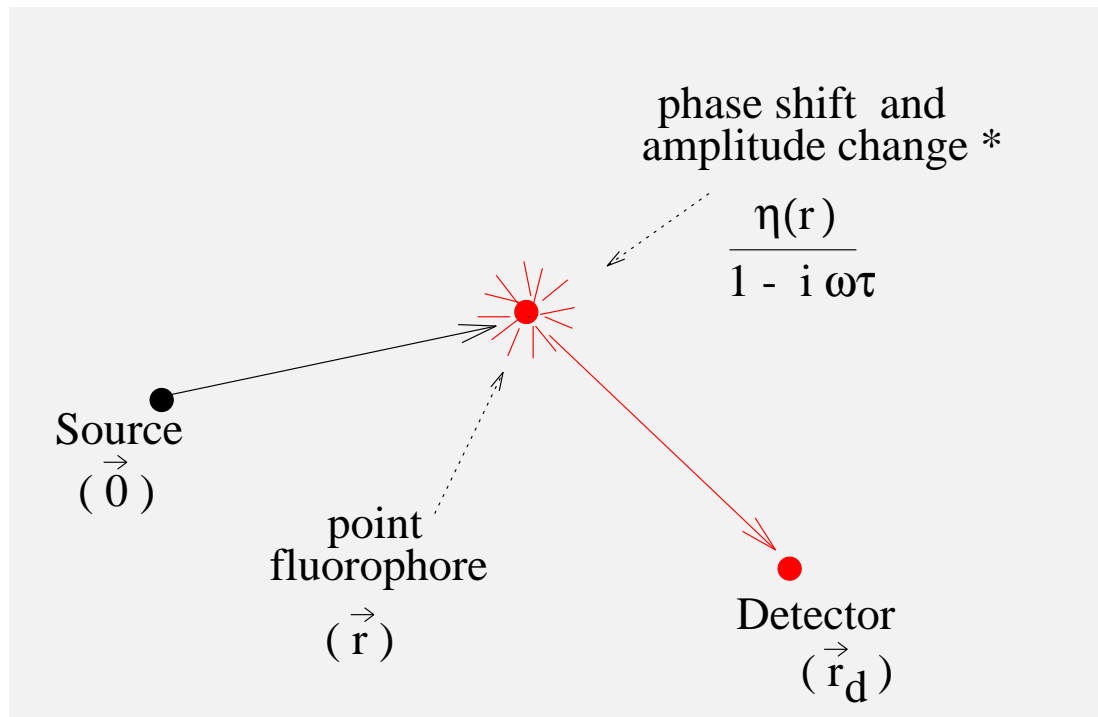


Figure 7.1: A schematic of fluorescent DPDW generation. A DPDW travels from the source to a fluorophore, and is demodulated due to the absorption and finite lifetime of the fluorophore. The fluorophore then acts as a source of fluorescent DPDW's.

## 7.2 Localizing Fluorescent Objects

In our first set of experiments we have observed the conversion or transduction of a diffuse photon density wave from one optical and diffusive wavelength to another [7, 11]. This was accomplished by illuminating an obstacle filled with ICG with a diffuse photon density wave. Because ICG has a lifetime of less than 1 ns compared to the 5 ns period of the source, the re-radiated energy was also in the form of a diffuse photon density wave that was readily detected at the Stoke-shifted energy. To localize the object we determine the source center from the re-radiated wavefronts.

Light is delivered into the sample through a source fiber, and is collected by a movable detector fiber. The primary results of our re-radiation experiments are shown in figure 7.2. Here the source laser is located at the origin and a 1.8 cm diameter transparent spherical shell filled with a 0.1% solution of Intralipid is located a distance of 4.5 cm from the source. The surrounding Intralipid has the same concentration, giving a photon diffusion constant,  $D = 6.0 \times 10^9 \text{ cm}^2/\text{sec}$ . ICG was dissolved in the spherical shell at a concentration of 0.41 mg/cc. The ICG absorbed light from the incident diffuse photon density wave at 780 nm, and then emitted photons at 830 nm. The absorption and emission characteristics of ICG are shown in figure 7.2a. Since the lifetime of the dye is relatively short ( $<1 \text{ ns}$ ), the re-radiated signal was also in the form of a diffuse photon density wave. Using spectral filters (2 back-to-back Schott glass filters, 3mm width, RG830, each with a transmittance of 0.003 at 780 nm and 0.46 at 830 nm) we separately measured the incident wave at 780 nm in the presence of the obstacle, and the re-radiated wave at 830 nm.

In 7.2b the constant amplitude contours of the diffuse photon density wave at 780 nm are presented in intervals that decrease by a factor of 0.3 with increasing distance from the source. We see that these contours are reasonably circular and can be extrapolated back to the laser source. The small deviations observed are primarily a result of absorption by the obstacle. A similar contour plot of the phase was also measured, and could also be extrapolated back to the laser source. The measured wavelength of the diffuse photon density wave in the homogeneous Intralipid was  $\approx 18$

cm.

In figure 7.2c we exhibit the constant amplitude contours of the wave at 830 nm, and thus demonstrate the diffuse photon density wave character of the re-radiated waves. We see clearly that the re-radiated wave originates from within the absorbing obstacle. From the contours we deduce a source origin which is within 1 mm of the center of the object. Similar conclusions could be drawn from the phase contours although the phase data was more sensitive to the small light leakages at 780 nm, and was therefore considerably noisier. This noise led to a diffuse photon density wavelength at 830 nm which was measured to be  $\approx 27$  cm, much larger than the wave at 780 nm. In subsequent experiments using the same system, we were able to decrease the leakage of 780 nm light by adding an additional filter and averaging longer. In these experiments we measured a wavelength which was about  $\approx 18$  cm as expected.

We have also compared re-radiated waves from spherical and cylindrical objects (see figure 7.3). The measurements clearly show that the contours in the case of the cylinder are more elliptical than those of the sphere, thereby demonstrating that the re-radiation technique can be sensitive to the shape of the obstacle.

A primary goal of our work is to develop an imaging device and algorithms for use in human subjects. In this section we discuss two imaging devices that we have developed, and localization in one or two dimensions is demonstrated [11].

The first device, shown in figure 7.4, uses multiple sources and a single detector to determine the center of a 1 cm diameter fluorescent sphere. We irradiate a fluorescent sphere with multiple time-shared sources of DPDW's, and then measure the amplitude and phase of the re-radiated light from each source. The partial amplitude resulting solely from source  $i$  is dependent on the  $i$ th source-detector separation, the efficiency of the dye,  $\eta$ , and the object-detector separation according to equation 7.7

$$U(\mathbf{r}_{si}, \mathbf{r}, \mathbf{r}_d, \tau, \omega) = U(\mathbf{r}_{si}, \mathbf{r}, \omega) \frac{\eta}{1 - i\omega\tau} U'(\mathbf{r}, \mathbf{r}_d, \omega) \quad (7.8)$$

where  $\mathbf{r}_i$  is the position of the  $i$ th source,  $\mathbf{r}$  is the position of the object center, and  $\mathbf{r}_d$  is the detector position. The individual sources are separately turned on and off,

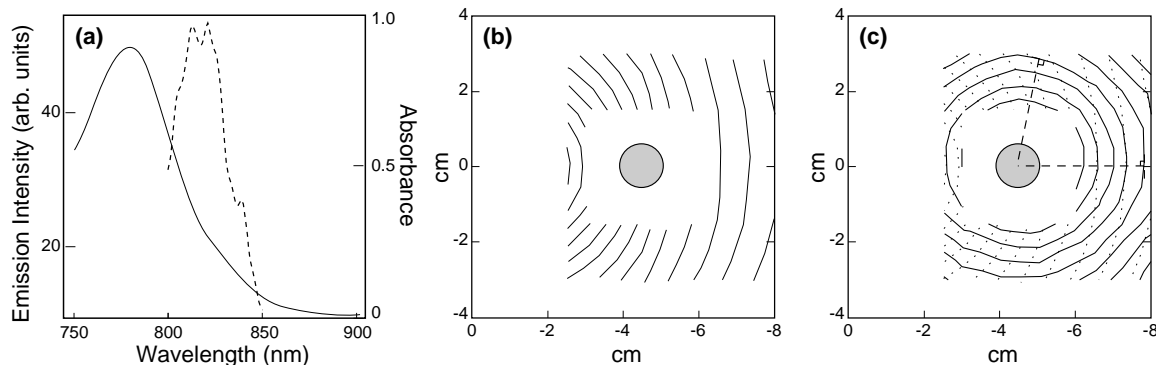


Figure 7.2: (a) Indocyanine green absorption (solid line) and emission (dashed line) spectra. (b) Constant amplitude contours of the incident diffuse photon density wave. (c) Constant amplitude contours at the fluorescent wavelength (solid lines) clearly exhibiting the re-radiated nature of the wave. The dashed lines are the incident amplitude contours, and the center of the radiator is located by finding the intersection of the lines normal to the re-radiated contours.

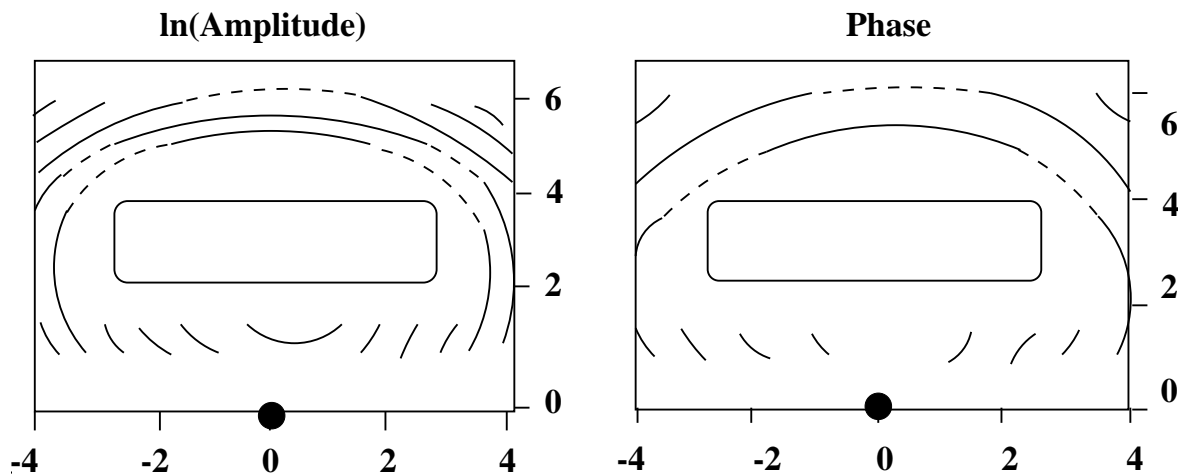


Figure 7.3: left: Constant amplitude contours of the fluorescent DPDW re-radiated from a cylindrical fluorescent object. The source is at the origin. The contours are drawn every 0.3 dBm. right: The contours of constant phase, drawn every  $10^\circ$ . The dashed lines are interpolated data.

and the re-radiated amplitude for each source-obstacle separation is measured. Since the source positions and the detector positions are known, we estimate the object position by finding the value of  $\mathbf{r}$  that gives the best agreement with the measured ratio  $|U_i|/|U_j|$ .

$$\frac{U(\mathbf{r}_{si}, \mathbf{r}, \mathbf{r}_d, \tau, \omega)}{U(\mathbf{r}_{sj}, \mathbf{r}, \mathbf{r}_d, \tau, \omega)} = \frac{U(\mathbf{r}_{si}, \mathbf{r}, \omega)}{U(\mathbf{r}_{sj}, \mathbf{r}, \omega)} = \frac{|\mathbf{r}_{sj} - \mathbf{r}| \exp(ik|\mathbf{r}_{si} - \mathbf{r}|)}{|\mathbf{r}_{si} - \mathbf{r}| \exp(ik|\mathbf{r}_{sj} - \mathbf{r}|)}. \quad (7.9)$$

Three sources are necessary to locate the object in two dimensions, we use four to improve the signal to noise of the localization. The results are shown in figure 7.5; the grey circle represents the actual position of the re-radiator, while the black dot is the computer estimated position. Using four sources we were able to localize the center of this 1 cm sphere to within 0.4 cm. This two dimensional localization is easily extended to three dimensions.

A second, qualitatively different imaging device is shown in figure 7.6. It uses a scanning phased-array and a single detector as discussed in section 2. The phased-array consists of two sources,  $180^\circ$  out of phase with respect to each other that interfere destructively to produce an amplitude null and a sharp  $180^\circ$  phase shift at the null line (broken line in insets of figure 7.6). If we place a detector on the null line, and then move an absorbing object from one side of the detector to the other, we find that the object preferentially absorbs light from the nearest source, and therefore distorts the null line. When the object is also a re-radiator, the complimentary effect is seen, that is, the object re-radiates more light derived from the closest source. In both measurements the phase of the detected DPDW will undergo a  $180^\circ$  shift as the object crosses the original, undisturbed position of the null line. These effects are demonstrated in figure 7.6a. Note that the re-radiated wave phase exhibits a complimentary phase change as discussed above. In our experiments we have scanned the object, but in the clinic it will be necessary to scan the pair and the detector simultaneously.

Interestingly, in the situation depicted in figure 7.6a, the location of the phase shift with respect to the null line of the re-radiated light is always the same, independent of the detector position. Thus we can detect essentially the same change by fixing

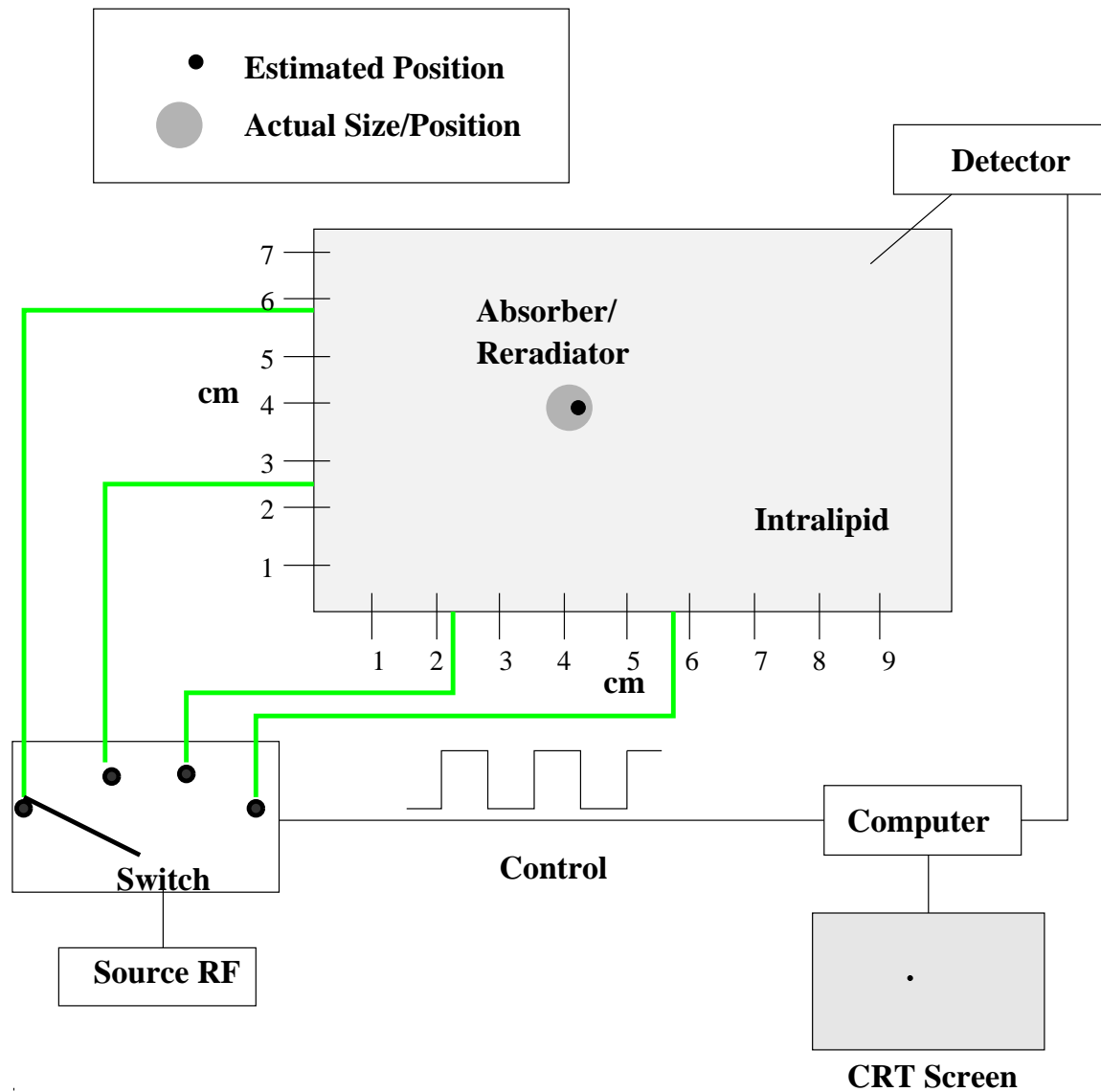


Figure 7.4: A device for localizing the center of a fluorescent object. The individual sources are separately turned on and off, and the re-radiated amplitude for each source-obstacle separation is measured. Since the source positions and the detector positions are known, we estimate the object position by finding the position that gives the best agreement with the theory.

## Localization of Absorber/Reradiator

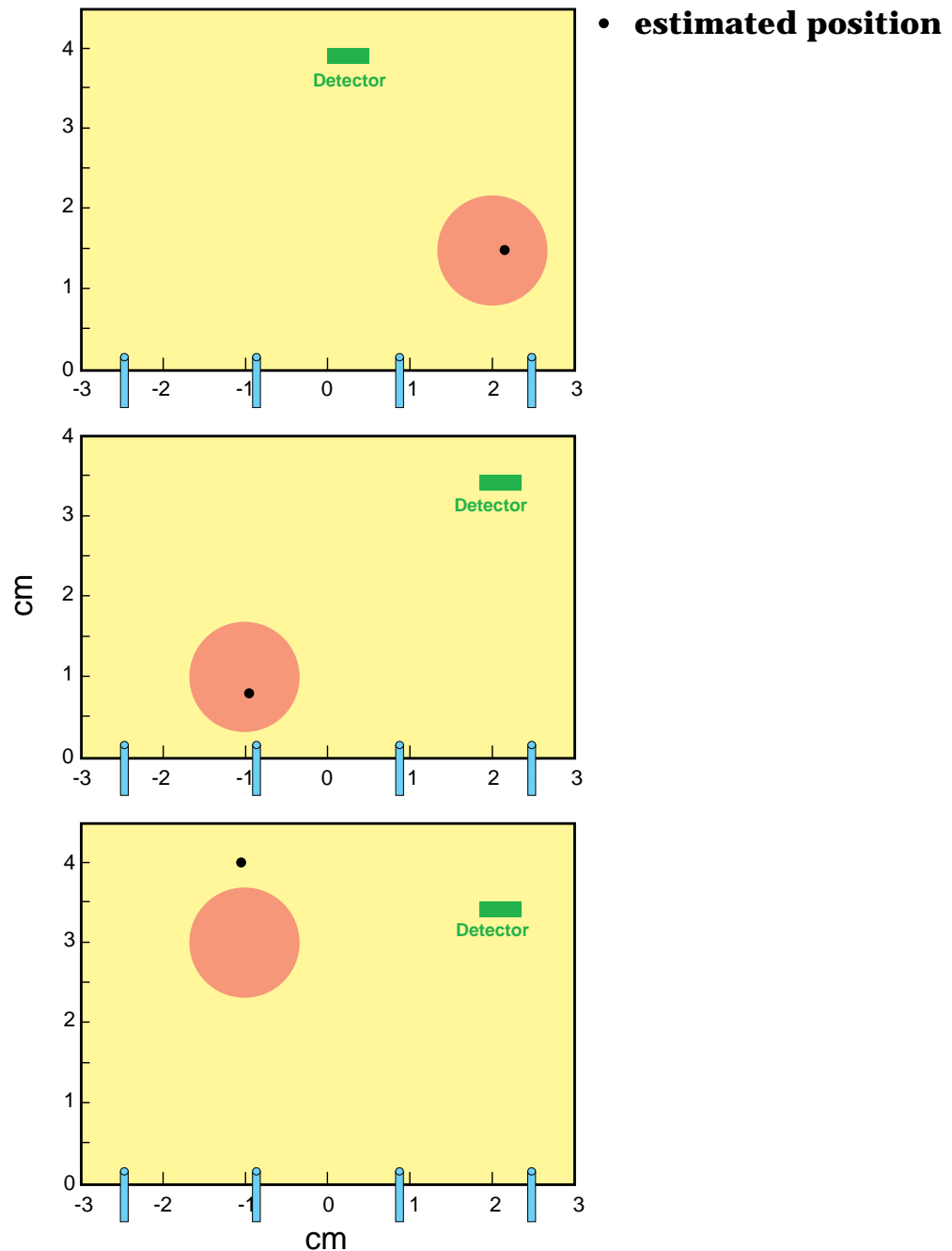


Figure 7.5: The actual size and position of the reradiator are shown by the shaded circles, and the estimated position using the fitting algorithm is shown by the black dot. Note that the algorithm has difficulty localizing an object which is far from the detection plane.

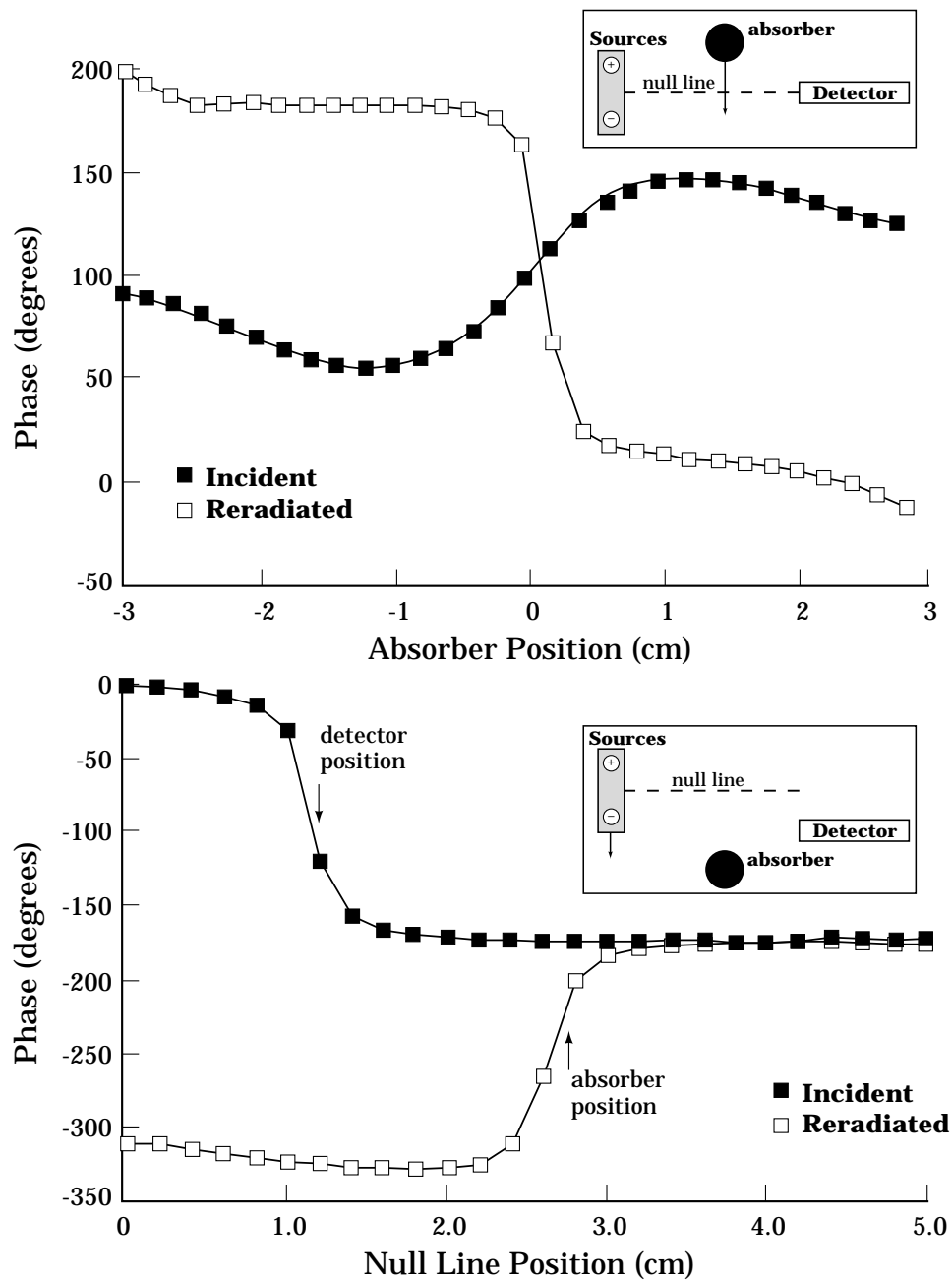


Figure 7.6: These experiments were performed with a 50 MHz oscillation frequency in a 0.4% Intralipid, with a source separation of 2.2 cm. The radiator was located 2.0 cm, and the detector 4.0 cm in front of two anti-phased sources. (a) As shown in the inset, the detector was placed on the null line (dashed line) and the radiator was scanned. In the main figure, both the incident and the reradiated light show a  $180^\circ$  phase shift, but the shift is sharper from the reradiated light. (b) Here, the source pair, and consequently the null line, was scanned as shown in the inset. Note that the sharp phase shift from the reradiated (incident) light occurs as the null line crosses the radiator (detector) position

the object and the detector, and scanning only the source pair. This configuration is more clinically realizable than the absorption case which requires scanning both the source pair and the detector. Figure 7.6b demonstrates this effect for the re-radiated light. In the left panel, we detect a sharp phase shift for the location of the re-radiator as we scan the null line. The phase shift of the incident light occurs near the position of the detector. If we know the position of the null line as a function of time, we achieve a one dimensional localization of the re-radiator. By performing three scans down three perpendicular axis, we can achieve three dimensional localization.

### 7.3 Tomographic Imaging of Fluorescent Objects

So far, we have discussed using diffuse fluorescence in deep tissues as a means of tumor detection and localization by imaging the *center* of fluorescing objects. In this section we demonstrate a more general method whereby one can simultaneously derive a spatial map of the concentration and lifetime of a fluorophore, using variations in the amplitude and phase of fluorescent diffuse photon density waves.

For a weakly absorbing spatial distribution of fluorophores, the fluorescent photon density wave is determined by integrating over the contributions from all fluorophores as in equation 7.7.

$$U_{fl}(\mathbf{r}_s, \mathbf{r}_d, \tau, \omega) = \int d^3r U(\mathbf{r}_s, \mathbf{r}, \omega) \frac{\eta(\mathbf{r})}{1 - i\omega\tau(\mathbf{r})} U'(\mathbf{r}, \mathbf{r}_d, \omega). \quad (7.10)$$

Note that we have allowed  $\eta$  and  $\tau$  to vary with position.

Hereafter we refer to  $U_{fl}$  as the fluorescent diffuse photon density wave. In a heterogeneous medium this model is an approximation in the sense that the homogeneous solution neglects the effects of heterogeneities on photon propagation from source to fluorophore and from fluorophore to detector. The model also assumes that there are no saturation or photon quenching effects.

The fluorescence model in equation 7.10 is of the same form as the first order Born approximation solution for a scattering medium with inhomogeneous absorption, i.e.

equation 4.13,

$$U_{sc}(\mathbf{r}_s, \mathbf{r}_d, \omega) = - \int U(\mathbf{r}_s, \mathbf{r}, \omega) O(\mathbf{r}) U'(\mathbf{r}, \mathbf{r}_d, \omega) d^3r. \quad (7.11)$$

Thus we are able to generate images for  $\eta(\mathbf{r})$  and  $\tau(\mathbf{r})$  using standard imaging algorithms. The reconstruction differs from the pure absorption case in that the reconstructed quantity is now complex, and is a function of the modulation frequency. Again, the reconstruction algorithm involves digitizing the integral in equation 7.10 ( $\eta(\mathbf{r}), \tau(\mathbf{r}), \mathbf{r} \Rightarrow \eta_j, \tau_j, r_j$ ), and for a series of measurements made at source-detector positions  $\mathbf{r}_{si}, \mathbf{r}_{di}$ , we generate the following matrix equation:

$$U_{fl}(\mathbf{r}_{si}, \mathbf{r}_{di}, \omega) = \sum_{j=1}^{N_{voxels}} U(\mathbf{r}_j, \mathbf{r}_{si}, \omega) \frac{\eta_j}{1 - i\omega\tau_j} U'(\mathbf{r}_{di}, \mathbf{r}_j, \omega) h^3. \quad (7.12)$$

This complex matrix is can be written as a real matrix;

$$\begin{pmatrix} \Re[U_{fl}^{[1]}] \\ \vdots \\ \Re[U_{fl}^{[m]}] \\ \Im[U_{fl}^{[1]}] \\ \vdots \\ \Im[U_{fl}^{[m]}] \end{pmatrix} = \begin{pmatrix} \Re[W_{11}^{fl}] & \dots & \Re[W_{1n}^{fl}] & -\Im[W_{11}^{fl}] & \dots & \Im[W_{1n}^{fl}] \\ \vdots & \ddots & \vdots & \vdots & \ddots & \vdots \\ \Re[W_{m1}^{fl}] & \dots & \Re[W_{mn}^{fl}] & -\Im[W_{m1}^{fl}] & \dots & -\Im[W_{mn}^{fl}] \\ \Im[W_{11}^{fl}] & \dots & \Im[W_{1n}^{fl}] & \Re[W_{11}^{fl}] & \dots & \Re[W_{1n}^{fl}] \\ \vdots & \ddots & \vdots & \vdots & \ddots & \vdots \\ \Im[W_{m1}^{fl}] & \dots & \Im[W_{mn}^{fl}] & \Re[W_{m1}^{fl}] & \dots & \Re[W_{mn}^{fl}] \end{pmatrix} \begin{pmatrix} \alpha(\mathbf{r}_1) \\ \vdots \\ \alpha(\mathbf{r}_n) \\ \beta(\mathbf{r}_1) \\ \vdots \\ \beta(\mathbf{r}_n) \end{pmatrix}$$

$$W_{ij}^{fl} = U(\mathbf{r}_j, \mathbf{r}_{si}, \omega) U'(\mathbf{r}_{di}, \mathbf{r}_j, \omega) h^3 \quad (7.13)$$

$$\alpha(\mathbf{r}_j) = \Re[\eta_j / (1 - i\omega\tau_j)] \quad (7.14)$$

$$\beta(\mathbf{r}_j) = \Im[\eta_j / (1 - i\omega\tau_j)] \quad (7.15)$$

This matrix equation can be inverted or solved using many techniques. We have used an algebraic reconstruction method (SIRT) to solve for the real ( $\alpha$ ) and imaginary ( $\beta$ ) parts of the unknown,  $\eta_j / (1 - i\omega\tau_j)$  [48]. The ratio of the imaginary to the

real parts of the solution yields  $\tau$ , and then  $\eta$  may be calculated.

$$\tau_j = \frac{\beta}{\alpha\omega} \quad (7.16)$$

$$\eta_j = \alpha + \omega\tau\beta \quad (7.17)$$

Computer generated data are obtained from exact solutions to the fluorescence diffusion equation for the case of a fluorescent sphere (1.0 cm diameter) in a uniform background [79]. Using forward amplitude and phase data from this solution (with added 1% amplitude and  $0.1^\circ$  phase noise), we have reconstructed images of  $\eta$  and  $\tau$ . The measurement geometry used is described in figure 7.9a. The scanning geometry consists of a source and detector scanning every 0.2 cm around the four sides of a 7.0 cm x 7.0 cm square in an infinite medium. The reconstruction area is a slab of area 5.0 cm x 5.0 cm and height 1.0 cm. The optical properties of the media are:  $\mu'_s = 10 \text{ cm}^{-1}$  everywhere,  $\mu_a$  (chromophore) =  $0.03 \text{ cm}^{-1}$  everywhere for both the excitation and the emission wavelength, and  $\mu_a$  (fluorophore - inside the sphere) =  $0.02 \text{ cm}^{-1}$  at the excitation wavelength, and  $0.01 \text{ cm}^{-1}$  at the emission wavelength. The source modulation frequency is 50 MHz. In the first set of reconstructions all fluorophores are located in the object and there is no background fluorescence.

In figure 7.9b we demonstrate a reconstruction proportional to the fluorophore concentration. The lifetime inside the 1.0 cm diameter sphere is 0.6 ns. The grey scale ranges from  $0 \text{ cm}^{-1}$  (grey) to  $0.007 \text{ cm}^{-1}$  (black). 2500 SIRT iterations were performed with a constraint on both concentration ( $0.0 \leq \eta \leq 0.1 \text{ cm}^{-1}$ ) and lifetime ( $0 \leq \tau \leq 10 \text{ ns}$ ).

Note that the reconstructed value of  $\eta$  is much less than the correct value. This is due to the fact that we have only performed 2500 SIRT iterations to produce this image. This relatively small number of SIRT iterations results in an image of a larger object with a lower concentration of fluorophores. This is exactly analogous to the absorption case where we discovered that as we increase the number of iterations, the reconstructed object becomes smaller and more absorbing. In the course of implementing these reconstructions we found that some isolated voxels had unphysically

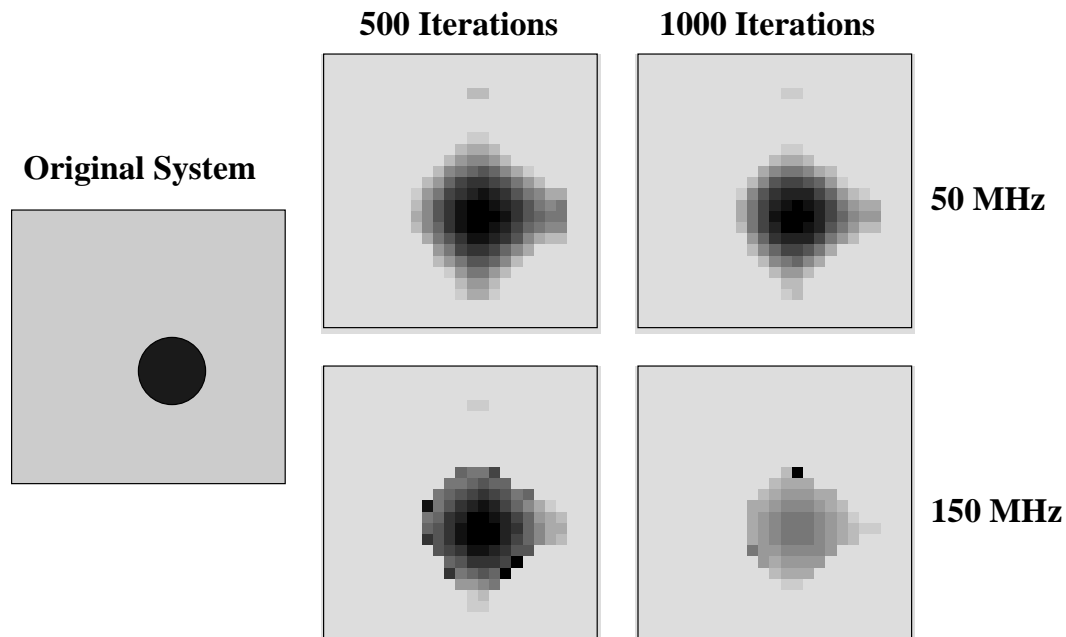


Figure 7.7: The top two images show the SIRT reconstructions at 500 and 1000 iterations using a 50 MHz source modulation. The bottom two images show the same reconstruction using a 150 MHz source modulation. Note that at the high modulation frequency, spurious voxels appear which have unphysically high values of  $\eta$  and  $\tau$ .

high values for both  $\eta$  and  $\tau$ . (These images look like a single voxel in a homogeneous background.) As we continue to iterate, our *image* becomes dominated by these voxels (see figure 7.7). However, these voxels do not contribute significantly to the total measured *signal* since the quantity  $\eta/\omega\tau$  is comparable to or smaller than that of the neighboring voxels. As part of our image analysis, we identified these voxels and replaced  $\eta$  and  $\tau$  with the nearest neighbor averages. Generally, we found that the lifetime reconstructions are more accurate at low source modulation frequencies where the occurrence of these spurious voxels is less frequent (see figure 7.7), and the phase shift due to the lifetime of the fluorophore ( $\phi = \tan^{-1}(\omega\tau)$ ) is far from its saturation value ( $\pi/2$ ) (see figure 7.8).

Using the same setup as in figure 7.9a, the actual lifetime of the fluorophore was varied from 0.5 ns to 1.5 ns, and the average reconstructed lifetime was calculated.

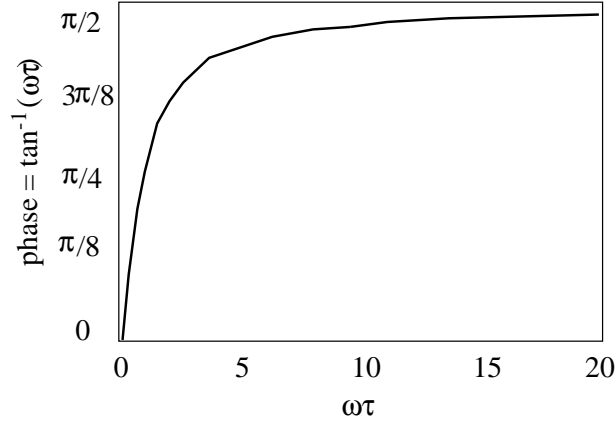


Figure 7.8: A plot of  $\tan^{-1}(\omega\tau)$  versus  $\omega\tau$  shows the saturation effect for  $\omega\tau$  greater than 1.

Figure 7.9c (squares) shows a good agreement between the average reconstructed value of the lifetime and the known value. The reconstructed lifetime is calculated by taking the average value over the area of the object. The area is taken to be any voxel with a fluorophore concentration greater than 50% of the maximum concentration.

The image quality is much improved if some *a priori* information is given. For example, if the fluorophore distribution is known, then we may focus solely on the lifetime inversion. Possible ways of determining the fluorophore distribution include using the excitation wave at a high modulation frequency, or using the zero modulation frequency fluorescence data. If we choose to use a zero modulation frequency (DC) source, then the equation describing the fluorescent DPDW is

$$U_{fl}(\mathbf{r}_s, \mathbf{r}_d, \tau, \omega = 0) = \int d^3r U(\mathbf{r}_s, \mathbf{r}, \omega = 0)\eta(\mathbf{r})U'(\mathbf{r}, \mathbf{r}_d, \omega = 0). \quad (7.18)$$

So using this equation we can reconstruct the quantity  $\eta(\mathbf{r})$ . However DC images traditionally result in low resolution maps, and it is unclear how well this approach will work in practice.

The results of the lifetime-only reconstruction for a 50 MHz source modulation are shown in figure 7.9c (circles). There is a slight improvement over the reconstructed values from the concentration and lifetime inversion.

Panels (d) and (e) are the same as (b) and (c), except the source modulation

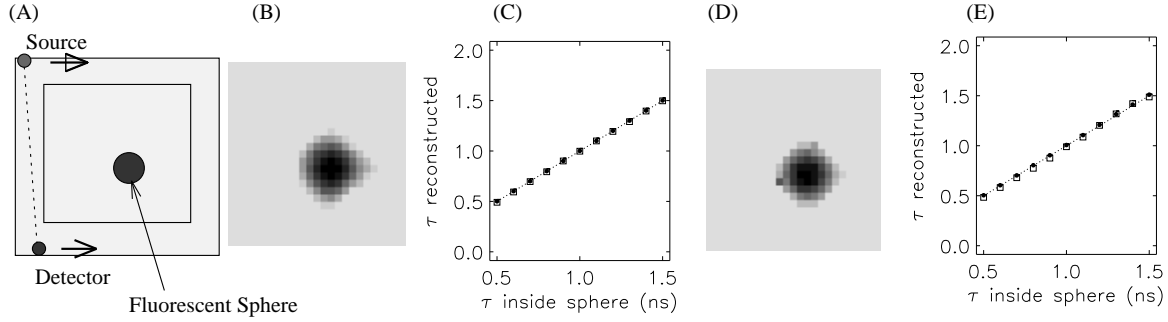


Figure 7.9: Reconstruction of fluorophore lifetime and concentration in a system with no background fluorophore. (a) Tee scanning geometry. (b) A sample concentration image. (c) The reconstructed lifetime for a series of reconstruction where the lifetime inside the sphere varied. The open squares are average lifetimes from a reconstruction of both concentration and lifetime, the solid circle are reconstructions in which the concentration was known, and only the lifetime was reconstructed. (b) and (c) are reconstruction using a 50 MHz source modulation, (d) and (e) are the same reconstructions using a 150 MHz source modulation.

frequency has been increased to  $f = 150$  MHz. The grey scale in panel (d) ranges from  $0 \text{ cm}^{-1}$  (grey) to  $0.009 \text{ cm}^{-1}$  (black).

Thus far our images have consisted of a region of fluorophore embedded in a non-fluorescent background medium. In typical clinical situations, there will also be a background concentration of fluorophore. In this case we separate the contributions from the uniform fluorescent background and the heterogeneous region as shown in figure 7.10, i.e.

$$\begin{aligned}
 U_{fl}(\mathbf{r}_s, \mathbf{r}_d, \tau, \omega) &= \int_{all \ space} d^3r U(\mathbf{r}_s, \mathbf{r}, \omega) \frac{\eta_o}{1 - i\omega\tau_o} U'(\mathbf{r}, \mathbf{r}_d, \omega) \\
 &+ \int_{heterogeneity} d^3r U(\mathbf{r}_s, \mathbf{r}, \omega) \left[ \frac{\eta(\mathbf{r})}{1 - i\omega\tau(\mathbf{r})} - \frac{\eta_o}{1 - i\omega\tau_o} \right] U'(\mathbf{r}, \mathbf{r}_d, \omega). \quad (7.19)
 \end{aligned}$$

$\eta_o$  and  $\tau_o$  are the background fluorescence properties (which exist only outside the heterogeneity) and  $\eta$  and  $\tau$  are the heterogeneity fluorescence properties. Hereafter we will refer to the first term on the right hand side of eq. 7.19 as  $U_{bg}$ . If the object contrast is high, i.e.  $\eta(\mathbf{r})/(1 - i\omega\tau(\mathbf{r})) \gg \eta_o/(1 - i\omega\tau_o)$ , then the fluorescent signal

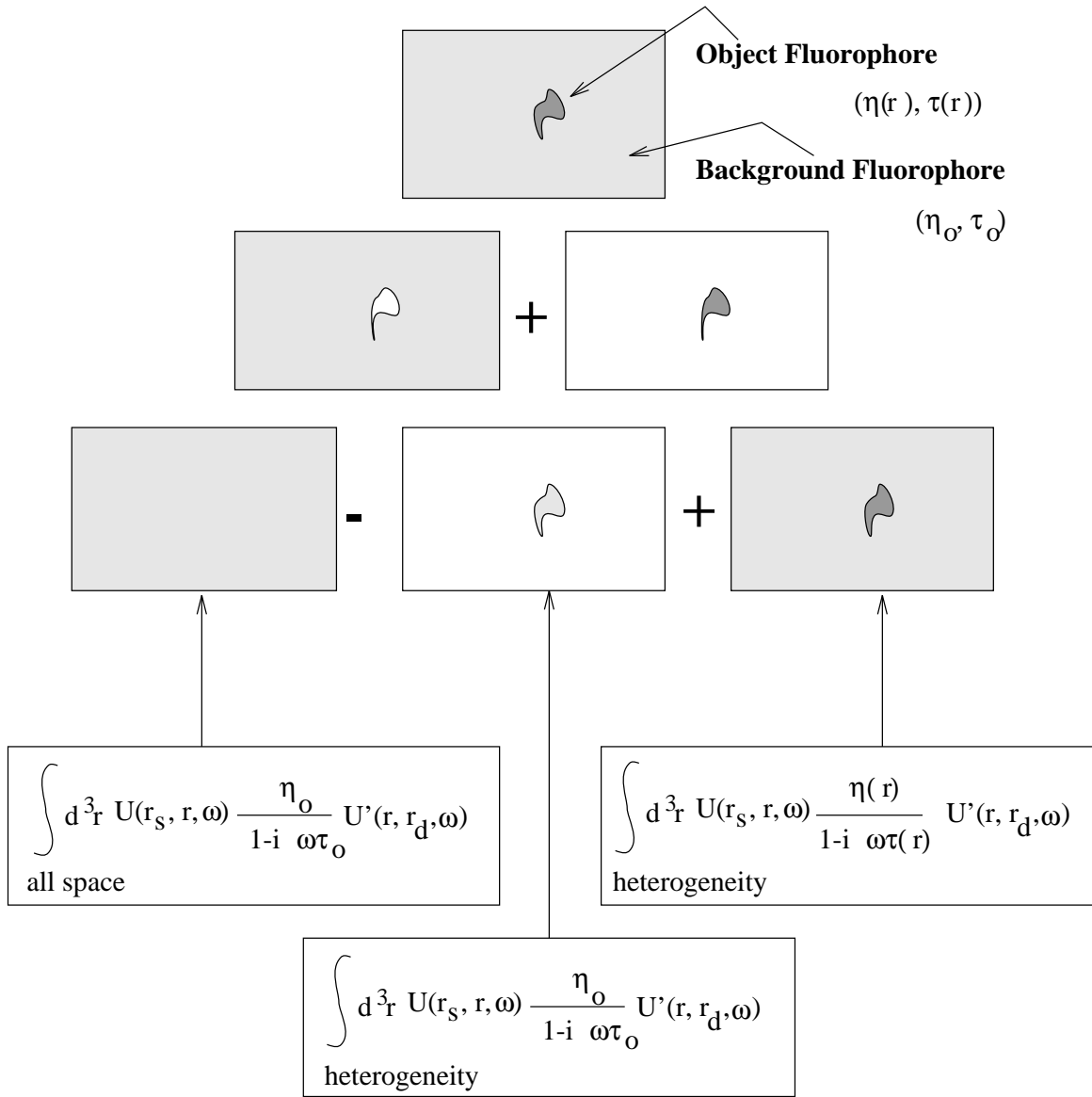


Figure 7.10: A cartoon describing the breakdown of the background fluorescence problem.

due to the heterogeneity,  $\Delta U_{fl} = U_{fl} - U_{bg}$ , is given by

$$\Delta U_{fl} = \int d^3r U(\mathbf{r}_s, \mathbf{r}, \omega) \frac{\eta(\mathbf{r})}{1 - i\omega\tau(\mathbf{r})} U'(\mathbf{r}, \mathbf{r}_d - \mathbf{r}, \omega). \quad (7.20)$$

To accomplish this subtraction, one may use analytic solutions for  $U_{bg}$  [79]. However this method requires knowledge of the background lifetime and concentration, which may not be possible in clinical situations. Another option is to eliminate the background signal by subtracting two measurements having the same source-detector separation, as shown in fig. 7.11a. In these *difference* measurements, the background (homogeneous) fluorescent contribution will cancel, and only the inhomogeneous part will remain. This is the same method we employed in absorption reconstructions to reduce the importance of accurate knowledge of the background optical properties [18]. Note that in these images the fluorescent properties of the heterogeneities have been reconstructed; no information about the background fluorescence lifetime is derived. We have however used the background fluorophore concentration in our calculation of the weights. If we incorrectly estimate the background fluorophore concentration, the reconstructed image will be degraded. One could envision an iterative routine to obtain the background fluorophore concentration in which the initial guess for the background fluorophore concentration is updated based on previous images until the clearest image is achieved. This approach, while extremely time consuming, could offer a more exact solution than our approach.

Figure 7.11d depicts the scanning geometry used for a system with fluorophore both inside and outside of the sphere (diameter = 1.5 cm). The setup is the same as in figure 7.9a with the addition of the background fluorophore and a second source 0.6 cm from the first, as shown in figure 7.11.  $\mu_a$  of the background fluorophore =  $0.001 \text{ cm}^{-1}$  at the excitation wavelength, and  $0.0005 \text{ cm}^{-1}$  at the emission wavelength and the lifetime is 1.0 ns. The reconstruction of the heterogeneous fluorophore distribution is shown in figure 7.11b for a system where the lifetime inside the 1.5 cm diameter sphere is 0.6 ns. The grey scale ranges from  $0 \text{ cm}^{-1}$  (grey) to  $0.017 \text{ cm}^{-1}$  (black). 2500 SIRT iterations were performed with a constraint on both concentration ( $0.0 \leq \eta \leq 0.1 \text{ cm}^{-1}$ ) and lifetime ( $0 \leq \tau \leq 10 \text{ ns}$ ).

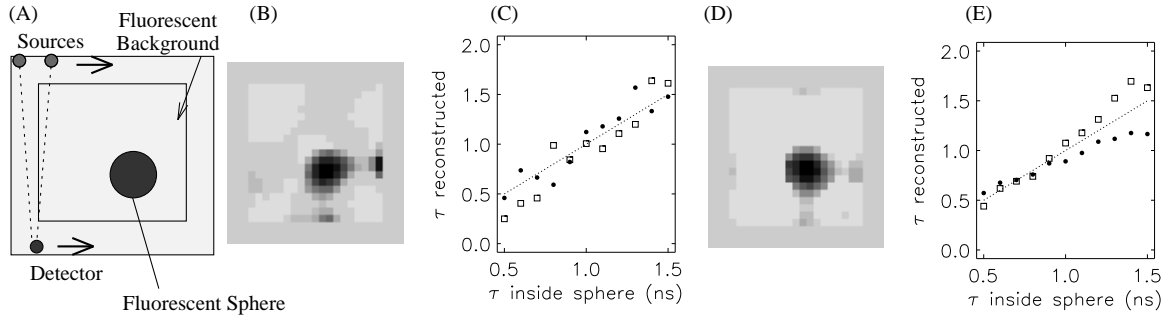


Figure 7.11: Reconstruction of fluorophore lifetime and concentration in a system with background fluorophore. (a) The scanning geometry. (b) A sample concentration image. (c) The reconstructed lifetime for a series of reconstruction where the lifetime inside the sphere varied. The open squares are average lifetimes from a reconstruction of both concentration and lifetime, the solid circle are reconstructions in which the concentration was known, and only the lifetime was reconstructed. (b) and (c) are reconstruction using a 50 MHz source modulation, (d) and (e) are the same reconstructions using a 150 MHz source modulation.

The average reconstructed lifetime for a series of reconstructions is shown in figure 7.11a. The squares are derived from a reconstruction of both fluorophore concentration and lifetime. The circles are derived from the lifetime reconstruction only. Panels (d) and (e) are the same as (b) and (c) except the source modulation frequency has been increased to  $f = 150$  MHz. The grey scale in panel (D) ranges from  $0 \text{ cm}^{-1}$  (grey) to  $0.020 \text{ cm}^{-1}$  (black).

We have presented and demonstrated an algorithm by which the heterogeneous fluorophore distribution and lifetime in a turbid medium may be obtained from tomographic measurements of near infra-red diffusing photon distributions. Although these reconstructions were carried out from data in the frequency domain, the results can also be obtained using Fourier transformed time domain data. The solution for finite systems may be obtained by applying the appropriate boundary conditions. Such solutions are readily available for a variety of geometries [59].

